5-2024

Environment and Response of 3D-Encapsulated Mesenchymal Stem Cells to Mechanical Loading

Augustus Greenwood
Washington University – McKelvey School of Engineering

WASHINGTON UNIVERSITY IN ST. LOUIS

McKelvey School of Engineering
Department of Mechanical Engineering and Materials Science

Thesis Examination Committee:
Lori Setton, Chair
Matthew Bersi
Amit Pathak

Environment and Response of 3D-Encapsulated Mesenchymal Stem Cells to Mechanical Loading

by

Augustus Greenwood

A thesis presented to
the McKelvey School of Engineering
of Washington University in
partial fulfillment of the
requirements for the degree
of Master of Science

May 2024
St. Louis, Missouri

Table of Contents

List of Figures

Acknowledgments

I am immensely grateful to have Professor Setton as an advisor and mentor. She graciously allowed me into her lab and patiently gave me the space to explore my interests. Additionally, my lab-mates have been amazing, I am so thankful for them answering my constant questions and always being willing to help.

I would not be here without my family. Their support, even from far away, is invaluable. Finally, I must express my very profound appreciation to my wife, Taylor, for providing me with unfailing love, support, and continuous encouragement. Her sense of humor makes the world a better place.

Augustus Greenwood

Washington University in St. Louis

May 2024

Dedicated to Taylor and to Lily

ABSTRACT OF THE THESIS

Environment and Response of 3D-Encapsulated Mesenchymal Stem Cells to Mechanical Loading

by

Augustus Greenwood

Master of Science in Materials Science and Engineering

Washington University in St. Louis, 2024

Professor Lori Setton, Chair

This thesis explores the micromechanical environment induced when cyclically compressing hydrogels via finite element modeling and experimentally on the impact of loading on mesenchymal stem cells (MSCs) when encapsulated withing 3D hydrogel matrices. Degenerative joint diseases, characterized by cartilage degradation, present significant challenges due to cartilage's limited self-repair capacity. Innovative approaches, including stem cell-based therapies and engineered biomaterials, have emerged as promising strategies for cartilage repair and regeneration. This work specifically investigates the calibration of a bioreactor, the uniformity of load response across the hydrogel constructs via finite element modeling (FEM), and the stress response of MSCs subjected to various dynamic loading conditions in an *in vitro* setting. Through FEM, it is shown that the immediate cellular environment is similar across waveforms. Additionally, the response is consistently separated into three spatial group of similar response, with varying size, regardless of the prescribed loading waveform. Finally, experimental analysis of loaded MSCs shows an increase in the medium nitrite concentration, indicating an elevated stress state. These studies create a platform to test and further understand MSC mechanobiology

as well as provides a framework for effectively modeling cellular environment with FEM and analysis of that output.

Chapter 1: Introduction

Musculoskeletal disorders significantly impact the economy, contributing to an average financial loss of around $300 billion due to healthcare expenses and loss of earnings just for arthritis [1]. Attempts to mitigate these diseases and enhance patients' quality of life has led to innovative research over the years. Notably, regenerative medicine presents promising avenues for addressing the irreversible damage to cartilage characteristic of arthritis, for which there remains no definitive cure. A pivotal focus of such innovation is the application of mesenchymal stem cells (MSCs), chosen for their immunomodulatory properties and relative abundance; however, both the delivery mechanism (i.e., biomaterials) and the environment when *in-vivo* (i.e., mechanical loading) are important areas of consideration. This thesis explores the potential of stem cell-based therapies to regenerate deteriorated cartilage, with particular attention to the role of mechanical loading in optimizing stem cell delivery to the affected tissues and joints.

Cartilage is a specialized type of connective tissue found throughout the body. It exists in three specialized forms with varying compositions of type II collagen and glycosaminoglycans: hyaline cartilage, the most common type of cartilage that distributes load and facilitates smooth joint movement; elastic cartilage, which stabilizes structures such as the ear and throat while maintaining flexibility; and fibrous cartilage, whose high tensile strength supports highly loaded tissues like the intervertebral disc [2]. Despite their different functions, these cartilage types each contain a single cell type, chondrocytes, which synthesize and maintain the extracellular matrix (ECM). Primarily composed of water, collagen fibers, and proteoglycans [3], the specific composition of the cartilage ECM determines the type of cartilage. In healthy cartilage, chondrocytes regulate the balance between the synthesis and degradation of matrix components; however, this balance is disrupted during cartilage degeneration, a characteristic of osteoarthritis.

In degenerative states, the catabolic activities of chondrocytes surpass their anabolic functions, leading to a net loss of matrix components [4].

Several factors contribute to the shift in chondrocyte behavior from anabolic to catabolic. First, excessive or abnormal mechanical loading on joints can induce chondrocytes to produce more catabolic enzymes such as matrix metalloproteinases (MMPs) and collagenases that degrade collagen and proteoglycans in the ECM [5]. This shift disrupts the delicate balance required for cartilage homeostasis and tissue integrity. Elevated inflammatory cytokines in osteoarthritic cartilage, such as interleukin-1β (IL-1β) and tumor necrosis factor-alpha (TNF-α), drive chondrocytes toward a catabolic state [6]. Oxidative stress is another critical factor that influences chondrocyte metabolism. Reactive oxygen species (ROS), which are often elevated in damaged or aging cartilage, can damage cellular components and further stimulate the production of catabolic enzymes while simultaneously inhibiting anabolic pathways. This oxidative damage can lead to chondrocyte senescence and apoptosis, accelerating cartilage degradation [7]. Aging also contributes to the shift from anabolism to catabolism in chondrocytes. As chondrocytes age, their capacity to produce and maintain the ECM diminishes, partly due to their reduced sensitivity to growth factors and anabolic stimuli. This decreased anabolic activity combined with an increased propensity for catabolic enzyme production contributes to the gradual degradation of cartilage observed in aging populations [8].

There is great interest in cell-based therapies that offer the potential to regenerate damaged cartilage by secreting various chemokines that potentially induce matrix production and reduce inflammation. However, there is evidence that injection of stem cells without a carrier result in leakage and could travel to unintended sites creating abnormal physiology such as osteophytes [9]. Biomaterials can be engineered to contain cells and inhibit their mobility, and to provide physical

and chemical cues that provide stimulation to the encapsulated cells [10]. These biomaterials aim to not only support cell growth and proliferation but also facilitate seamless tissue integration, thereby enhancing the efficacy of cartilage repair strategies.

MSCs are of interest for tissue engineering and regenerative medicine. MSCs are multipotent cells found in various tissues, including bone marrow, adipose tissue, and umbilical cord blood [11]. They can differentiate into a variety of cell types crucial for tissue repair and regeneration such as osteoblasts, adipocytes, and chondrocytes [12]. Their immunomodulatory properties can also suppress immune responses while promoting tissue healing [13]. Moreover, MSCs have proven successful in preclinical and clinical studies for various medical conditions, including osteoarthritis and autoimmune disorders [14], [15], [16]. However, further research is needed to fully understand the behavior of delivered MSCs in the physical environment of the degenerated joint to optimize material design for clinical applications.

Biomaterials can be designed to create a supportive microenvironment for delivered cells that enhances cell survival, proliferation, and differentiation post-transplantation [17]. In some cases, biomaterials can be engineered to replicate the physical and chemical properties of the ECM, serving as a scaffold foundation that promotes several critical aspects of cell health. By simulating the ECM's complex structure and biochemical composition, these innovative materials can provide an environment conducive to cell adhesion, proliferation, and differentiation [18]. For example, it has been shown that stiff ECM promotes osteogenic differentiation compared to softer matrices [19]. One class of biomaterial for cell delivery is hydrogels because of the ability to tune porosity, degradation kinetics, and bioactivity [20] for specific tissue types and therapeutic goals, thereby advancing the efficacy and clinical translation of regenerative therapies.

Bioactive peptides can be conjugated to the backbone of hydrogels to further enhance cell behavior and differentiation, exemplified by the arginine-glycine-aspartic acid (RGD) peptide. This peptide enhances biomaterial-mediated cell delivery for tissue repair due to the RGD sequence being a key recognition motif for integrins, which are crucial for cell adhesion to the extracellular matrix (ECM) and promote cell activity [21]. By integrating RGD peptides into biomaterials, these structures can more accurately mimic the cellular microenvironment, promoting integration with host tissues and supporting tissue regeneration. RGD-functionalized scaffolds have thus been successfully applied to regenerate various tissues through specific cell-material interactions [22], [23]. This strategy highlights the advancement of biomaterials in tissue engineering, setting the stage for incorporating mechanotransduction considerations."

In addition to the biomaterials used for encapsulation, mechanotransduction plays a pivotal role in guiding the behavior of MSCs, especially in the context of regenerative medicine. This process converts mechanical stimuli into biochemical signals that direct key cellular activities, such as migration, proliferation, and differentiation [21]. Mechanosensors like integrins, alongside signaling pathways such as focal adhesion kinases and the YAP/TAZ complex, are instrumental in this conversion [22]. These components not only facilitate the dynamic adaptation of MSCs to their biomechanical environment but are also vital for optimizing therapeutic strategies aimed at effective tissue regeneration. An enhanced understanding of these pathways is crucial for designing biomaterials that replicate the native cellular environments, thereby promoting the successful integration and functionality of implanted cells.

Finally, mechanical loading is an important consideration; it is highly prevalent *in-vivo* and significantly influences both the behavior of MSCs and the structural properties of biomaterials. Integrating controlled mechanical loading regimes into 3D culture systems enables researchers to

examine how mechanical stimuli affect MSC behavior and facilitate the replication of the native tissue environment. Notably, mechanical loading has been shown to increase medium nitrite concentration, indicating that such loading may elevate oxidative stress in MSCs [24]. Understanding and accounting for these mechanical loads are crucial when considering the injection of MSCs for cartilage regeneration, ensuring that the therapeutic benefits are maximized while minimizing potential adverse effects.

This thesis aims to investigate how mechanical loading and peptide conjugation affect MSCs encapsulated in a 3D hydrogel matrix. Chapter 2 discusses the calibration for the bioreactor used to apply load to the cell systems. Chapter 3 investigates the microenvironment produced in the material of interest for cell delivery. The homogeneity of the construct response when under cyclic compression between different waveforms is explored using finite element modeling and cluster analysis. Finally, Chapter 4 explores how mechanical loading affects MSCs encapsulated in 3D hydrogels modified with cell-adhesive peptides.

Chapter 2: Bioreactor Calibration

2.1 Materials and Methods

Compression was performed using a custom-built, 24-well bioreactor as described previously [23]. The device consists of a stepper motor with a mounted optical encoder for closed-loop displacement control. Stepper motor movement was controlled using custom code written in Rust interfacing with an Arcus Performax NSC-A1 stepper motor controller. All code used to communicate with the control box and move the stepper motor can be found hosted on GitHub [24]. **Figure 2.1** shows the bioreactor used in this study and its individual parts. Briefly, a stepper motor at the top of the base, is controlled by the motor control box. The motor drives a threaded rod which linearly translates a stage. To apply load to each well, a platen holder with 24 sites to hold platens was attached to the stage.

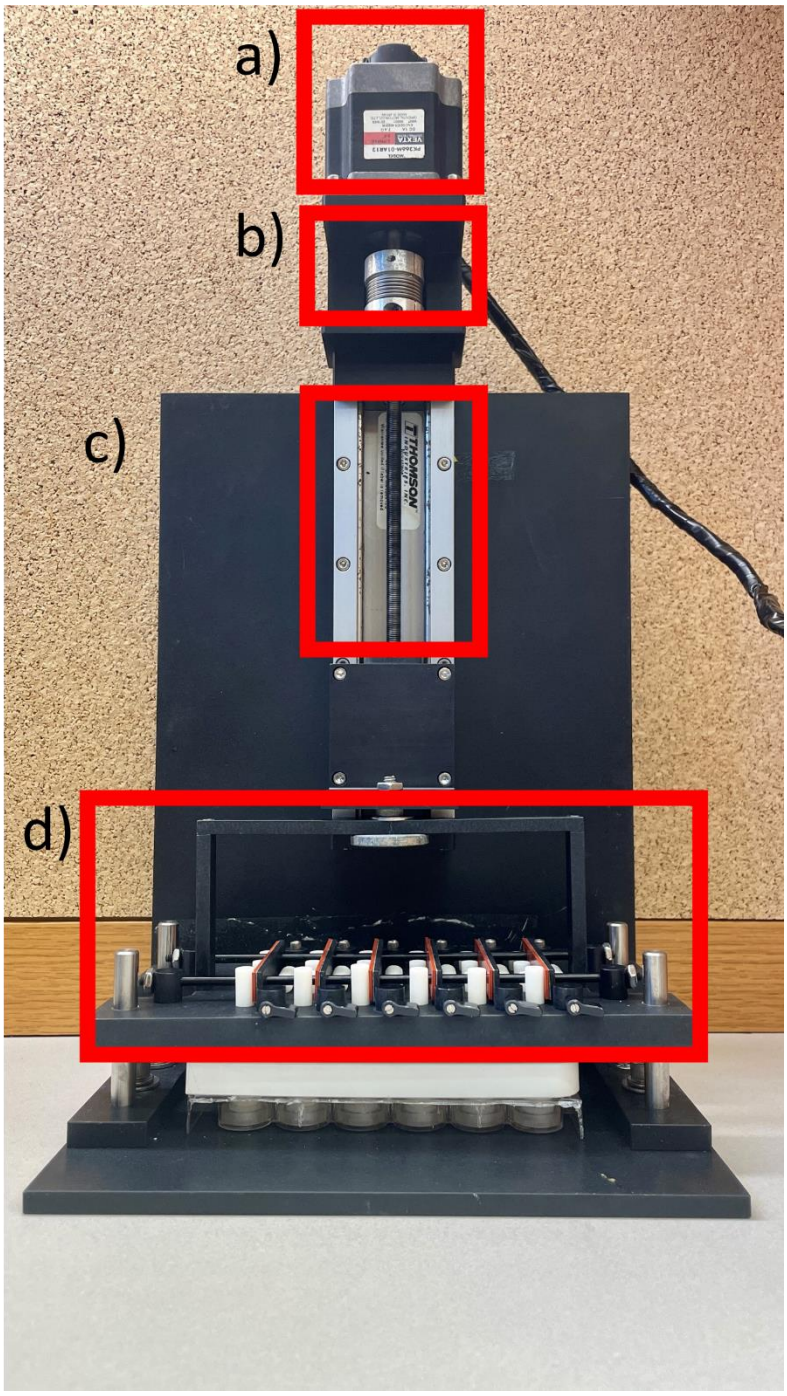

Figure 2.1: A schematic of the bioreactor. a) stepper motor b) motor-rod attachment c) threaded rod, and d) platen holder.

To validate the movement of bioreactor, images were taken at the apex of its movement for a programmed ramp and hold waveform to track movement in pixels which were converted to millimeters using an instrumented ruler. The waveform prescribed to the bioreactor is displayed in **Figure 2.2**.

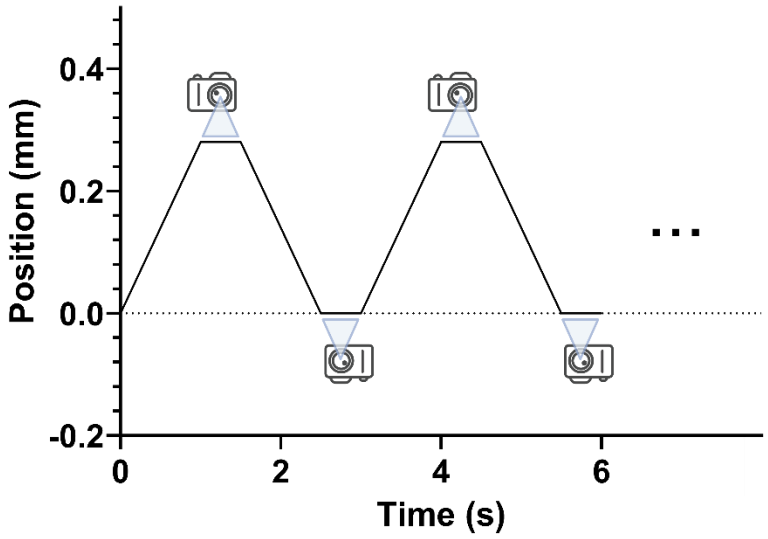

Figure 2.2: Waveform prescribed for movement validation with indication of points where pictures were taken.

Custom code using OpenCV in C++ was written to analyze 24-bit images with three color channels. After conversion to 8-bit grayscale images, all template matching and convolution were performed on a specific region of interest (ROI) in each image. **Figure 2.3** shows a representative original image alongside the cropped and grayscale image used for all analyses. All code for image analysis can be found hosted on GitHub [25].

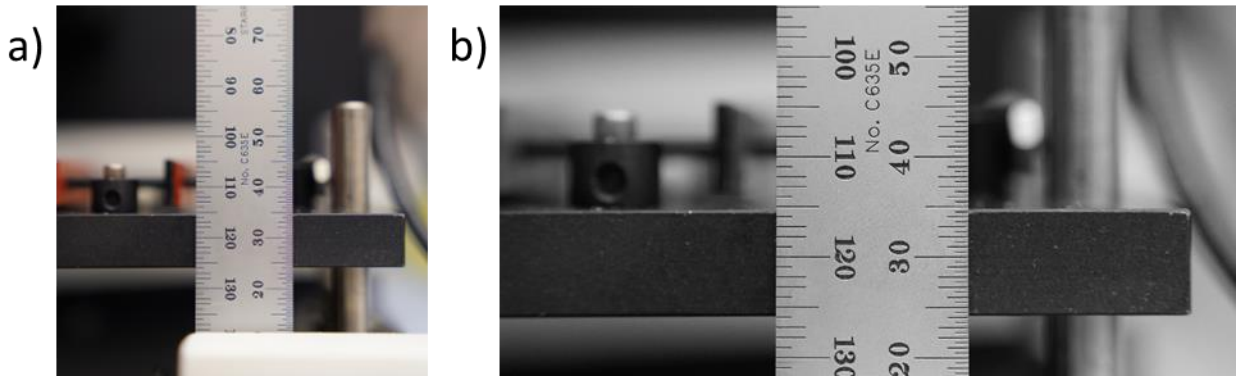

Figure 2.3: a) Original color image taken at each movement apex and b) the resulting cropped grayscale image used for subsequent analysis.

2.2 Results and Discussion

First, the camera's pixel count was calibrated to a millimeter distance by applying a y-derivative Sobel filter to the cropped grayscale image of the instrumented ruler shown in **Figure 2.4a**. Thresholding of the image was then performed after convolution to place all absolute values below 255 as the background and 255 to the foreground. Finally, a column of pixels that intersected with the ruler lines was extracted. By counting pixels between successive peaks, the pixel distance between ruler markings was extracted to obtain a pixel-to-millimeter conversion. **Figure 2.4** shows how the images were analyzed to extract the conversion factor. The distance between peaks in **Figure 2.4c** was averaged, yielding a conversion factor of 0.0120±0.0002 mm/pixel. This resolution was sufficient but not ideal for discerning distances in this study. If additional studies are performed, a calibration pattern would be useful to both get a more accurate conversion from world coordinates to camera and obtaining the camera matrix.

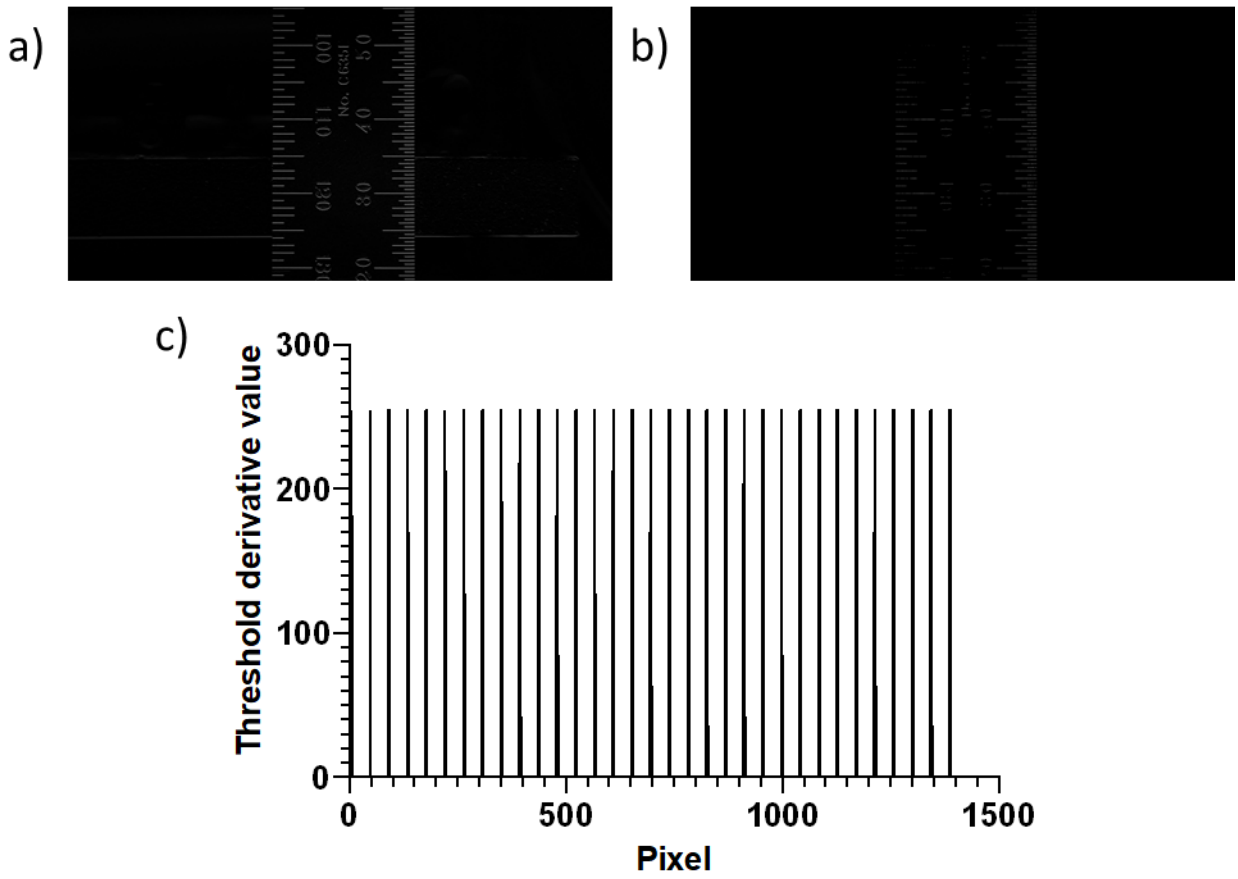

Figure 2.4: a) y-derivative Sobel filter b) thresholded y-derivative Sobel filter. c) Distance between ruler lines discerned by thresholded image.

The relative relationship between prescribed pulse movement and physical distance traveled was determined by first moving the stage at 4806 pulses followed by the next multiple of 4806 eight times. Template matching and a normalized cross-correlation algorithm were performed to track the movement of the stage. **Figure 2.5** shows the original picture with the defined template (a) along with the location of best match for the final movement (b). The distinguishing feature used in the template was a large circular bore in the platen holder, as the random markings on the side of the platen holder were neither large nor random enough to reliably find the location of best

match in each image. Using this feature, the algorithm found the location of best match with a response greater than 0.98 for all images. **Figures 2.5c–d** show heatmaps of the cross-correlation results for the first and final image.

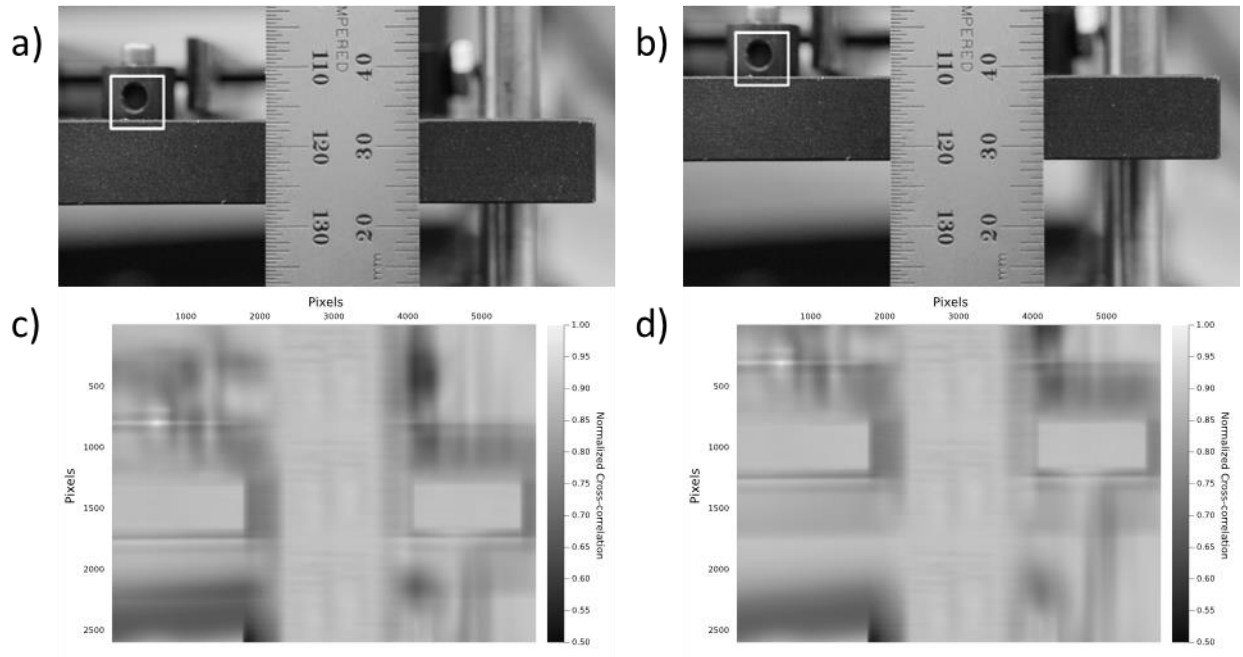

Figure 2.5: Template matching for the (a,c) first image and (b,d) final image with the matched template region (a,b) and heatmap for the cross-correlation value (c,d). With a value of 1 indicating a total match and 0 being no similarity

Figure 2.6 shows the resulting curve from the movement of the stage, plotting pixel movement versus prescribed pulse movement. The relationship enables interpolation to pulse values different from those explored in a cycle in this study. Successive movements and their respective physical movement were in linear agreement. As was observed when investigating repeated movement in a cycle, movement distance was consistent for extended periods of time;

however, to better evaluate this relationship, repeated movements at a certain pulse count can be used.

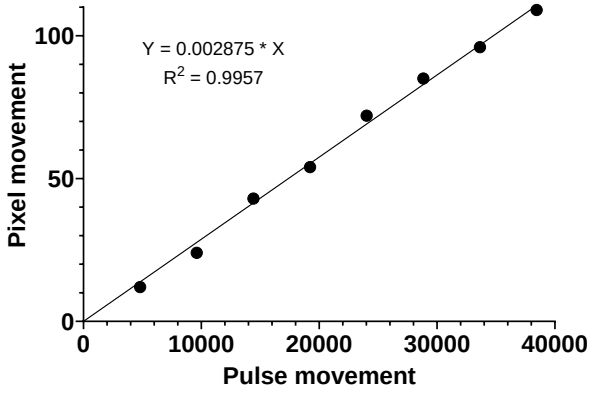

Figure 2.6: The linear relationship between prescribed pulse movement and the resulting movement in pixels.

Template matching using a normalized cross-correlation algorithm was also performed to track the movement of the stage at each apex of movement. A ROI in the first image that was completely contained within the edges of the platen holder was chosen as the template. The edge of the platen holder facing the camera featured a series of identifying marks to enable template matching. **Figure 2.7** shows the results of template matching for two representative images at each apex of the loader movement. Although there is a region of high response around the location of best match, template matching produced responses greater than 0.99 for all 100 images.

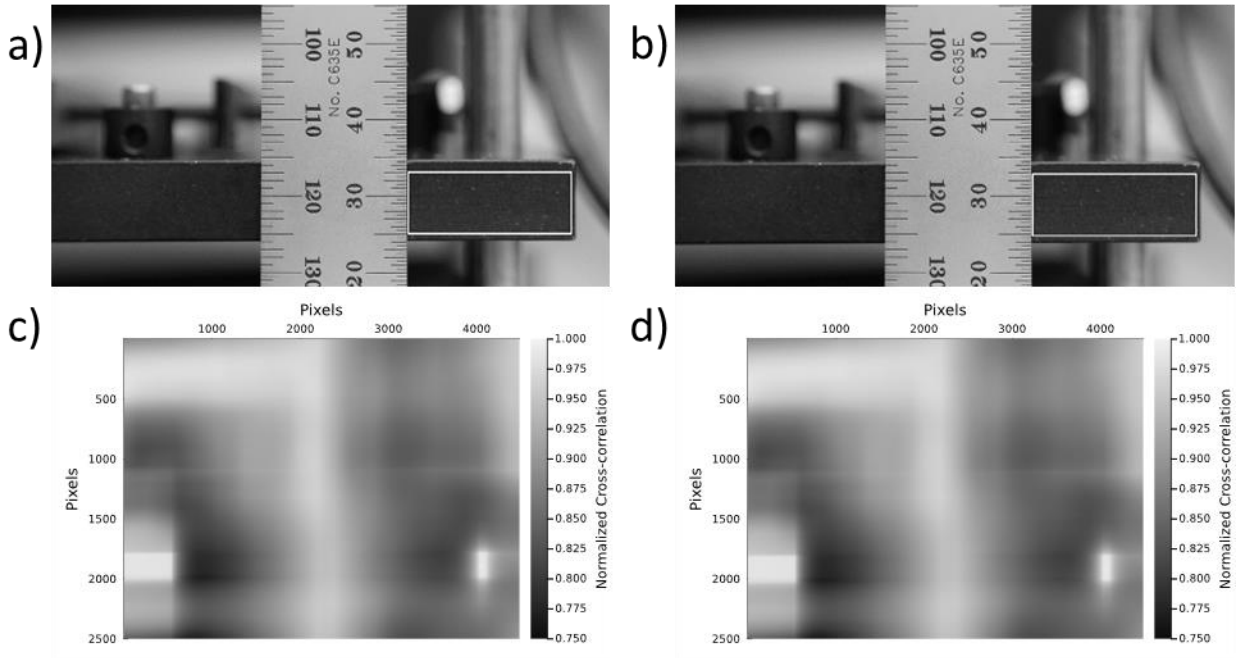

Figure 2.7: (a, b) Template matching-generated responses at the two apex positions. (c,d) Heatmap values for the normalized cross-correlation algorithm. With a value of 1 indicating a total match and 0 being no similarity

Template matching used a random pattern visible on the platen holder, but the pattern is not ideal. Though it appears to be unique, the pattern is too small relative to the resolution of the image. To alleviate such problems related to the resolution of the pattern, the template region was enlarged to capture a greater number of features to match. Still, **Figures 2.7c–d** reveal a large region of high response, which could introduce variability in the predicted location of best match. **Figure 2.8** shows the movement over the entire calibration procedure. Movement varied but never excessively missed the prescribed location.

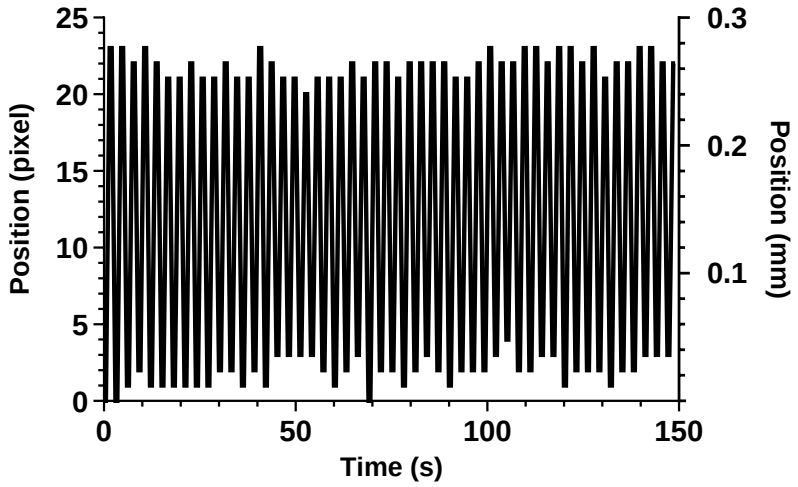

Figure 2.8: Movement of stage over 50 cycles in pixel and millimeter distance.

The bioreactor was calibrated in the time domain without the use of external devices. **Figure 2.9** shows the general procedure for this calibration. Briefly, the stepper motor moves continuously with a constant dwell time and changing ramp speed. At every three cycles, the average cycle time is calculated, for those three cycles. If that cycle time is within 0.05s of the desired cycle time, calibration ends, and the final ramp speed is output to be used in a loading run. If the calculated cycle time is too long, ramp speed is increased, conversely if the cycle time is too short, ramp time is decreased. Dwell time is never adjusted in the calibration procedure or during runs. In loading runs, a similar procedure is used to keep the loader moving at a consistent period; however, ramp speed is adjusted every cycle instead of every three cycles. Using this procedure, measured cycle time never deviated from the prescribed cycle time by more than 0.1s. All time measurements were performed using build-in functions to the Rust languages featuring nanosecond precision [26].

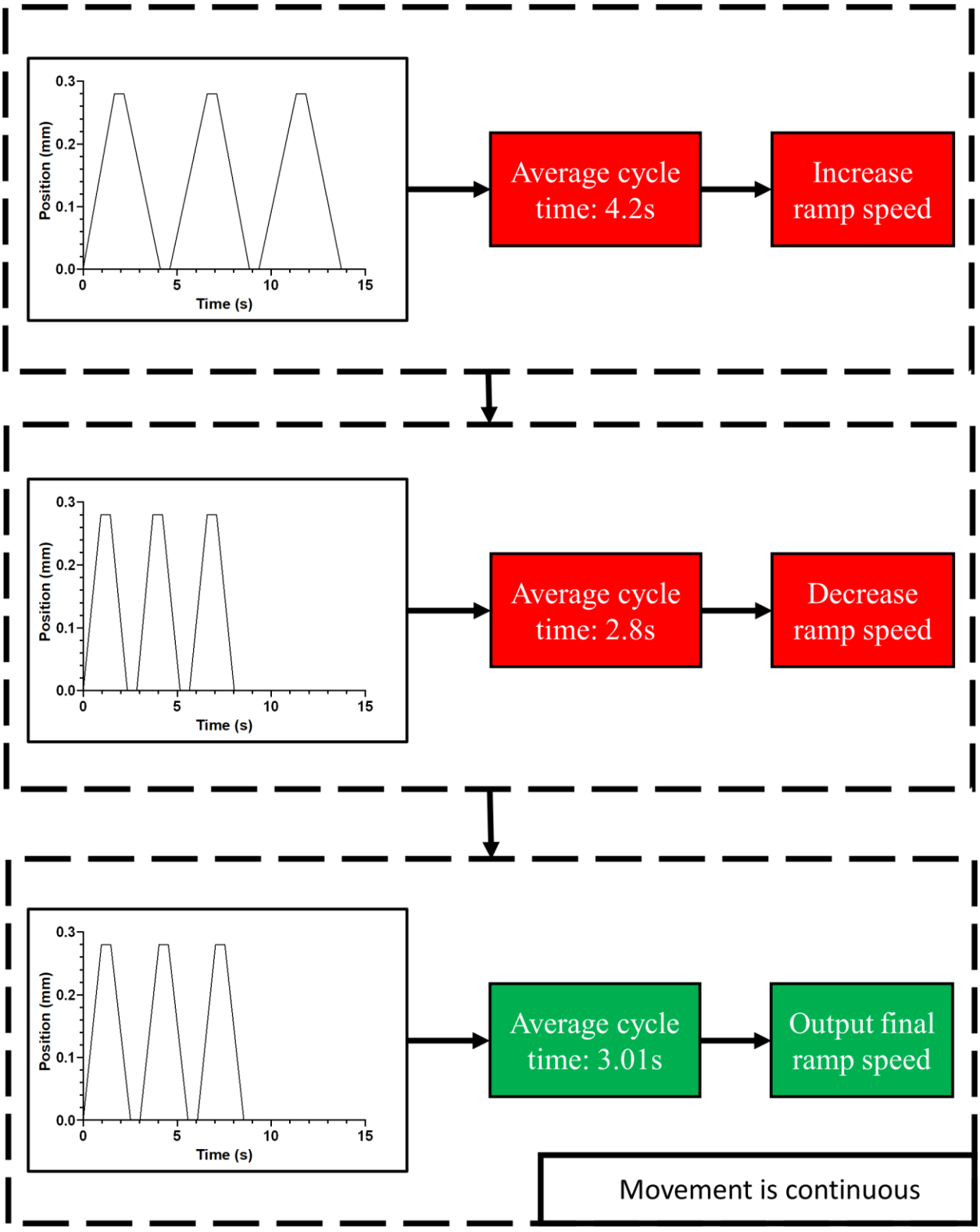

Figure 2.9: Temporal calibration flow-chart depicting an example calibration taking nine total cycles at the end of which the ramp speed is output.

2.3 Conclusion

This chapter described the calibration of a bioreactor in both the temporal and spatial domain. The method used to calibrate the camera was not ideal; a calibration pattern is preferred. However, pixel number converted to millimeter distance gave rise to a resolution adequate for the mechanical loading of stem cells performed in this study. The linear relationship between prescribed pulse movement and pixel distance traveled showed good linear agreement within the range explored. Additionally, the stage was moved through 50 cycles, and the deviation between the prescribed pulse movement and final position was within tolerance. Despite some variation in cycles, the stepper motor controller effectively stayed within a tolerable range for the compression of cell-laden hydrogels over prolonged periods.

Chapter 3: Uniformity of load response

3.1 Introduction

Finite element modeling (FEM) is a computational technique to simulate and analyze the effects of physical forces on various structures; in the realm of biomechanics, it enables researchers to predict the behavior of various tissues, including bones and soft tissues, under different loading conditions. It has been extensively applied in biomechanics for analyzing stress and strain, quantifying mechanical properties and predicting fracture load [27].

The cellular environment plays a crucial role in mechanobiology, influencing cell behavior and fate [28]. Understanding how cells sense and respond to mechanical cues in their environment, such as hydrostatic pressure, strain and fluid flow, will be of critical importance to understanding cell function in various environments [29]. Hydrostatic pressure has been shown to increase aggrecan and collagen II in MSCs [30]. Shearing strains and direct mechanical stretch can induce stretching of the cytoskeleton by the ECM, with significant effects on cellular behaviors [29]. Fluid flow causes both shear stress on the cell and supports nutrient transport.

Many studies report using a sinusoidal waveform or only a cyclical waveform for a variety of types of loading [31], [32], which is ambiguous; moreover, especially when using devices like stepper motors, a true sinusoid is difficult to reproduce. Stepper motors move in discrete steps, so the continuous acceleration required to produce a sinusoid is variable. Thus, more reliable waveforms are needed to enhance studies on the mechanical loading of cells. One such waveform that may more accurately represent a loading cycle experienced *in-vivo* is a trapezoid. A trapezoid cycle would involve a linear ramp up, a short dwell, linear ramp down, and a final dwell. Such linear ramps and holds are also easier to reproduce than a sinusoid.

The data extracted from FEM can be large; therefore, data cluster analysis can help reduce the dimensionality of the data. One such clustering algorithm is k-means clustering, which has been adapted for various applications beyond traditional data analysis. For example, the implementation of k-means for clustering large datasets like single-cell RNA-sequencing data highlights its adaptability and potential for handling complex datasets [33].

This chapter describes efforts to predict the microenvironment at different spatial positions in a hydrogel under dynamic compressive loading. Utilizing three trapezoidal waveforms and a sinusoid with FEM analysis to predict the cellular microenvironment under load at varying regions within the hydrogel construct. The FEM output will be clustered through k-means clustering to reduce dimensions for comparison and characterize the spatial uniformity of the generated physical stimuli.

3.2 Materials and Methods

FEM of the loaded construct (FEBio [34]) was performed to identify a waveform that would maximize the uniformity of the pressure, fluid flux, and strain in the construct. A quarter symmetry of a cylindrical hydrogel construct with height 1.5mm ($h = 1.5mm$) and diameter 6mm ($r = 3mm$) was modeled as adherent to top and bottom platens but with free-draining conditions on the radial periphery. The construct was meshed with Hex8 and Penta6 elements and modeled as biphasic with neo-Hookean material properties and strain-independent isotropic hydraulic permeability. The material properties necessary to model the system were: solid-volume fraction (φ^s), Young's modulus (E), Poisson's ratio (ν), and hydraulic permeability (k). Importantly, alginate is modeled as a biphasic material, encompassing a solid and fluid phase. The parameters E and ν are defined for the solid matrix only. For the purposes of this study all necessary parameters needed

were determined from previous work. The values used for all models were: $\phi^s = 0.044$ [35]; $E = 0.00475\ MPa$ [36]; $\nu = 0.27$; $k = 0.64\frac{mm^4}{N \cdot s}$ [35]. Poisson's ratio was not found directly, it was calculated using the aggregate modulus [35] and elastic modulus. **Figure 3.1** demonstrates the model used for this study, for the experimental system.

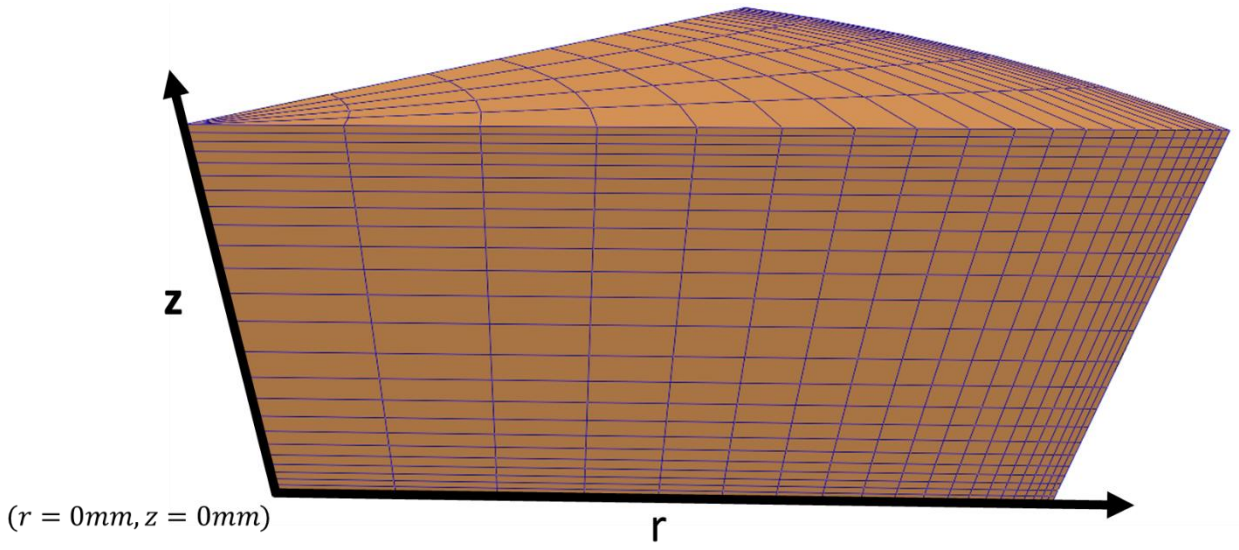

Figure 3.1: Construct used in FE model, with mesh, to explore microenvironment of hydrogels under loading. Model shown without rigid platens and with r and z direction definitions.

Compression was applied to the construct by a rigid body to simulate the experimental conditions for multiple trapezoidal waveforms and a sinusoidal waveform at 0.33 Hz. The model was first verified by analytical solutions for confined compression (CC) and unconfined compression (UC) FE models; this was performed to find an appropriate mesh for the experimental system, as no closed-form solutions to UC with adherent interfaces exist for verification.

CC and UC models had the same material properties as the experimental system. However, the necessary boundary conditions to model the system varied. Briefly, CC required a zero fluid pressure boundary (free draining) on the $z = 1.5mm$ surface, whereas UC required a zero fluid pressure boundary at the $r = 3mm$ surface. For CC, the $r = 3mm$ surface was fixed from any normal displacement, while UC had no restriction on that surface. The floor was not explicitly modeled in either system to reduce computational costs. Instead, the surface at $z = 0$ was constrained from any movement in the z-direction. CC was performed with a constant surface force applied at $z = 1.5mm$. For UC, all nodes at $z = 1.5mm$ were prescribed a vertical compressive displacement. The vertical displacement of this surface at equilibrium was the same for both systems, 0.075mm. This corresponded to a 5% ($v(\infty)/h$) compressive strain. For the experimental system, loading was performed with a 5% compressive strain static offset with an 8% compressive strain dynamic cycle superimposed. The experimental system was carried out to steady state, around 600s, at which point model predictions of key variables, 1st and 2nd strain invariant (J_1, J_2), fluid flux magnitude (w), and hydrostatic pressure (p), were extracted at specified times in a cycle.

To determine the uniformity of the construct under load, k-means clustering was performed on nodal output. The input to k-means clustering featured a 4x546 matrix composed of 546 nodes along a slice of the construct and four chosen nodal variables (J_1, J_2, w, p). Each row of the matrix was scaled to ensure all four rows were of a similar order; the chosen scaling function divided each row by its standard deviation. To compare across waveforms, the scaling function calculated the standard deviation across the rows of all waveforms being compared, for that variable. The resulting scaled data matrix was inputted into the k-means algorithm, and the output was a 546-element vector with an integer assigned for each node. All nodes belonging to a particular

assignment were a “cluster”. The reported response of a cluster represented the geometric average of all nodes assigned to that cluster. For the purposes of this study, cluster number was determined by running the algorithm with three, four, and five clusters. Data is reported with three clusters, as node assignment was inconsistent and heavily influenced by the initial placement of the cluster center when using more than three clusters.

3.3 Results and Discussion

Before modeling the experimental system, the density and computational efficiency of the mesh were optimized. This often involves comparing responses from the FE model to derived analytical solutions; however, the experimental system of interest in Chapter 4 is an UC problem with a perfectly adherent load surface for which no analytical solutions exist. Therefore, direct verification was not possible. To verify the experimental system, two separate but similar problems were modeled and verified: confined and unconfined compression. These two systems have well established analytical solutions against which FE model predictions can be verified.

CC and UC required mesh densities in different directions; specifically, mesh density needed to be concentrated at the free-draining boundary because of the zero-fluid pressure condition. Additionally, in each system, the direction perpendicular to primary fluid flow did not require any mesh divisions. Thus, any radial or axial mesh divisions would not have enhanced the accuracy of the CC or UC systems, respectively. The UC, CC and experimental model systems featured five mesh divisions along the azimuthal direction.

UC and CC feature the use of a characteristic time parameter, t_g, which is used to scale and nondimensionalize the time of simulation. It is also be referred to as “gel diffusion” time. This

parameter is defined differently for the two-system depending on the direction of fluid flow. The form of this parameter is $h^2/H_a k$ for CC and $a^2/H_a k$ for UC. Where h is the height of the construct, a is the radius, H_a is the aggregate modulus and k is the hydraulic permeability. The gel diffusion time represents the relative time it takes for a solvent to diffuse through the polymer matrix. Most importantly is the dependence upon the permeability and length of the longest path a solvent must take (height in CC and radius in CC), and the permeability. With the hydraulic permeability being a measure of the ease a solvent passes through a solid matrix. It is observed that for both UC and CC, a system will reach equilibrium between around 1.5-2.0 "gel times".

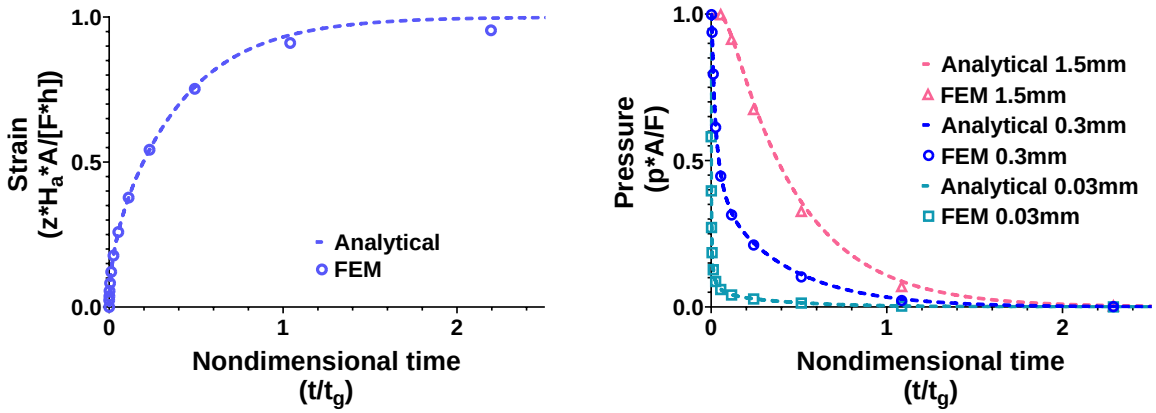

Figure 3.2: Results for confined compression demonstrating agreement between FE predictions and analytical solutions for a) axial strain and b) pressure. Pressure is plotted at different axial depths, i.e. distance from top axial face.

CC was modeled with 20 mesh divisions along the axis of the construct with a 0.85 bias, meaning that each element was 85% the length of the previous, decreasing element size as height increased. **Figure 3.2** shows good agreement for the axial strain and pressure along the depth of the construct. The FE model is slightly stiffer than the analytical solution given its slight

attenuation in the total strain at equilibrium; however, the analytical solution assumed a linear modulus of elasticity for the solid matrix, whereas the FE model featured neo-Hookean properties producing a non-linear modulus, especially at higher strains.

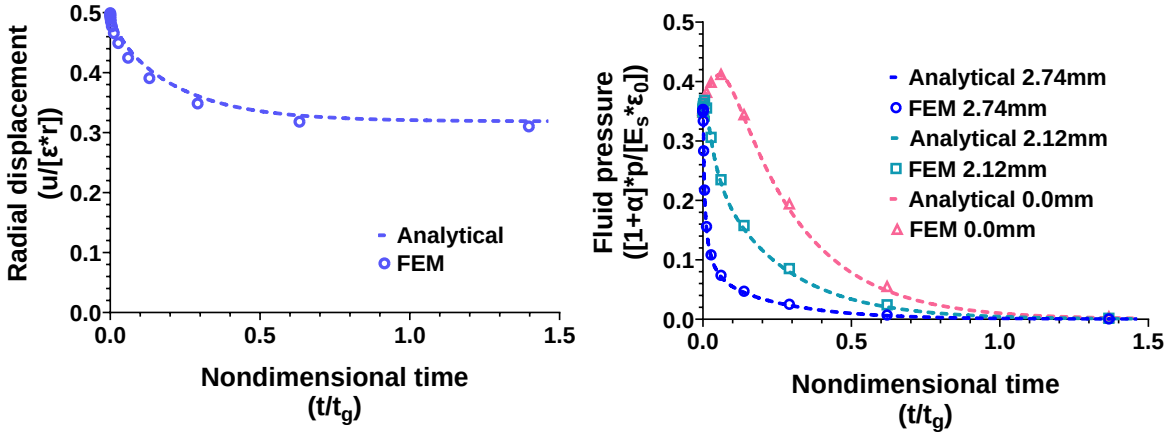

Figure 3.3: Results for unconfined compression demonstrating agreement between FE predictions and analytical solutions for a) radial displacement and b) fluid pressure. Fluid pressure is plotted at different radial positions, i.e. distance from center of construct.

UC was modeled with 20 mesh divisions along the radial direction of the construct with a 0.85 bias, decreasing element size as the distance from the construct center increased. **Figure 3.3** shows the agreement between UC FE model and analytical solution. As observed in the CC system, the FE model was slightly stiffer than the analytical solution. This can be observed by greater recoil in the radius at equilibrium. However, there is good agreement in the fluid pressure over time at different points in the construct's radial direction. This mesh structure was similarly implemented in the experimental system.

In the experimental system for Chapter 4, there were assumed perfectly adherent contact interfaces at both axial surfaces. This required a bias mirrored at the center of the construct translating to the smallest element sizes located at the top and bottom surfaces. To account for this extra requirement, five mesh divisions were added in the axial direction for the experimental system. The experimental system was appropriately meshed and loaded with four different waveforms. As discussed previously, a sinusoid is a commonly reported waveform when loading encapsulated cells, but a trapezoidal waveform may be a better choice because of its easier execution with a stepper motor. Accordingly, the model was loaded with four waveforms: a sinusoidal and three trapezoidal waveforms. The three trapezoidal waveforms had the same period but different dwell times. **Figure 3.4** shows the four waveforms whose effect on the homogeneity of the system was investigated.

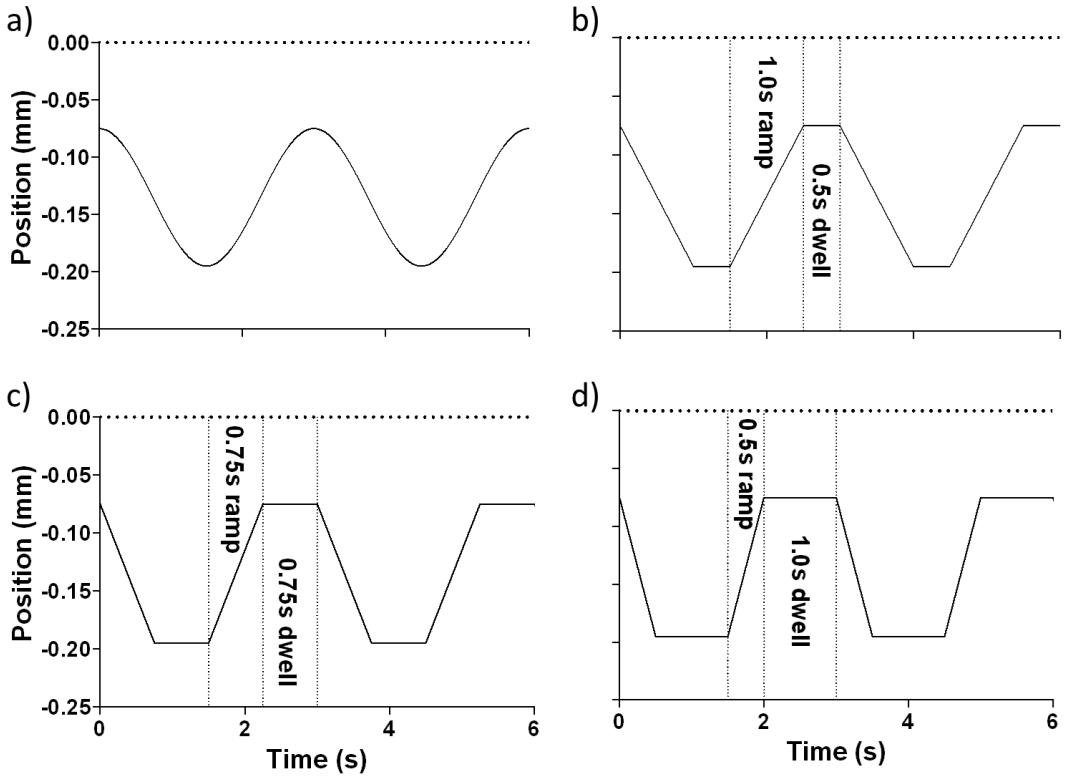

Figure 3.4: Four waveforms explored in this study: a) sinusoid b) 0.5s dwell trapezoid c) 0.75s dwell trapezoid and d) 1s dwell trapezoid.

It is not efficient nor necessary to compare all waveforms at all timepoints for the entire model spatially. It is more effective to compare the times at which the systems each reach a dynamic equilibrium. Given the cyclical nature of the loading, variables would similarly fluctuate. To effectively compare, dynamic equilibrium was defined as when the investigated variables did not change more than 1% between successive peaks. This was about 600s for all waveforms. The variables chosen to extract from the FE model were those experimentally shown to affect cellular response: strain (shear and volumetric), hydrostatic pressure, and fluid flow.

To reduce the dimensionality of the comparison, cluster analysis was performed for each waveform at two different timepoints. Each node (or point in space on the model) could be compared across every waveform, but this would not be tractable to make any definitive statement; instead, cluster analysis reduced the problem from four 4x546 matrices to four 4x3 matrices. These resulting matrices are composed of a four-element vector containing the average response of all nodes belonging to a cluster. These vectors with nodal averages simplified comparisons across waveforms. **Figure 3.5** shows the comparison of the average node response by cluster; here the standard deviation plotted represents the variability for that variable in the geometric region corresponding to the cluster. Variables were scaled across all waveforms.

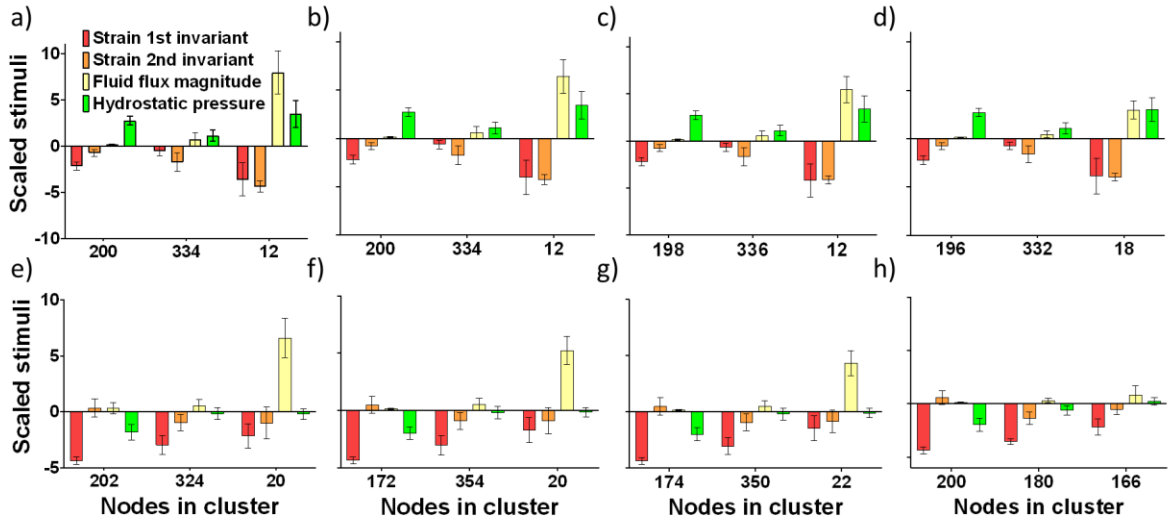

Figure 3.5: Comparison of the scaled response of each cluster at end of compression (a–d) and end of relaxation (e–h) for 1s dwell (a,e), 0.75s dwell (b,f), 0.5s dwell (c,g), and sinusoid (d,h). Data across all waveforms at a particular timepoint are presented as mean ± std of every node belonging to a particular cluster. Bars are arranged from left to right by increasing radial center of mass of the cluster.

Figure 3.5 shows that the response at the end of compression was similar for all waveforms; moreover, any noticeable differences occurred only in the cluster at the radial periphery. Of note is that the only major difference between trapezoidal waveforms for both end of compression and end or relaxation was the fluid flux magnitude. The fluid flux also increased with dwell time. This follows the reasoning of fluid flux being related to the speed of deformation. To accommodate the same period, waveforms with longer dwell must have shorter and much quicker ramps. Thus, the sharp decrease in the fluid flux in the sinusoid waveform is reasonable. Compared to a sinusoid with no dwell, its gradual accelerations led to much lower fluid flux magnitudes. It is apparent, however, that the most homogeneous trapezoidal waveform is one with a 0.5s dwell time. To better compare conditions, the most homogeneous waveforms, sinusoid and 0.5s dwell trapezoid, were compared and shown in **Figure 3.6**. Data was rescaled to cover only the two waveforms being compared.

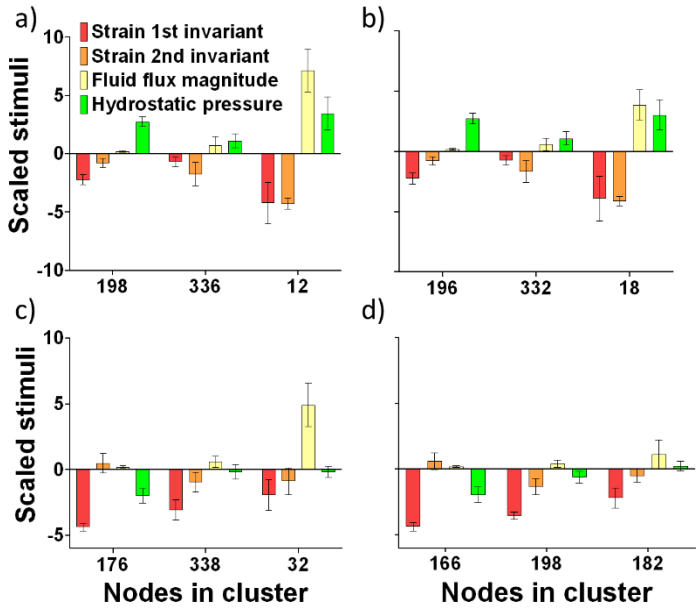

Figure 3.6: Comparison of 0.5s dwell (a,c) and sinusoid (b,d) for end of compression (a,b) and at end of relaxation (c,d). Variables were scaled by only the two waveforms presented.

Figure 3.6 displays that for end of compression, there was no appreciable difference except for the final radial cluster fluid flux magnitude; however, such a difference is much less pronounced. Conversely, there were large differences in the fluid flux at end of relaxation. As discussed previously, the sinusoid's gradual deceleration/acceleration would produce a much lower fluid flux. There was also a large difference in the number of nodes assigned to a cluster at end of relaxation. While these results show that the construct is consistently separated into three major regions by response regardless of waveform, the size of that region may fluctuate.

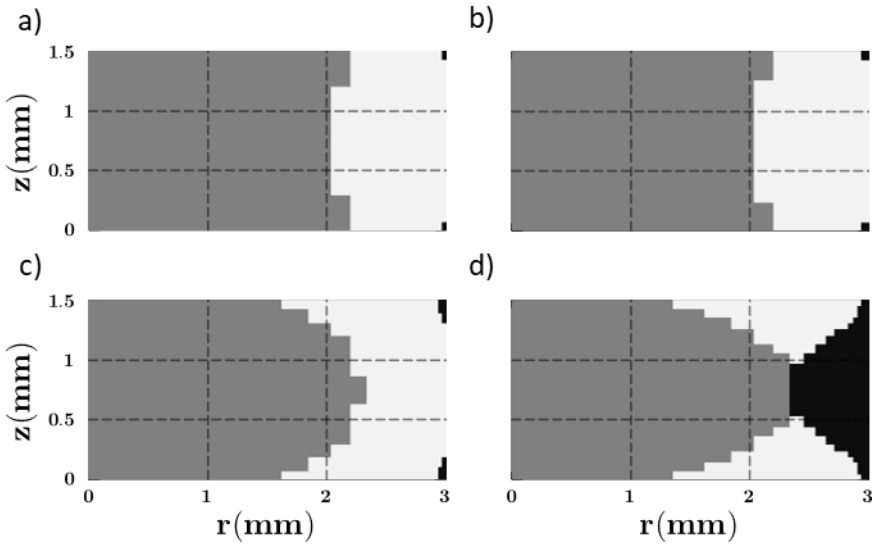

Figure 3.7: Comparison of which nodes belonged to a cluster in a construct for 0.5s dwell (a,c) and sinusoid (b,d) for end of compression (a,b) and at end of relaxation (c,d). Variables were scaled by only the two waveforms presented. Importantly, there is no relation between clusters of the same color in different waveforms or timepoints; placement is dependent only on a single waveform and timepoint.

To clarify the distribution of mechanical responses within the hydrogel construct, the spatial assignment of nodes to specific clusters was analyzed in **Figure 3.7**. The figure uses color coding to indicate the location of each cluster within the construct. At the end of compression, two clusters showed almost identical positions and responses (as seen in **Figures 3.7a-b** and **3.6a-b**). The third cluster, highlighted by a notable change in fluid flux (**Figure 3.6a-b**), occupied a small area of the construct. Consequently, its impact on the overall cellular response within the construct would be minimal.

Upon examining the construct at the end of relaxation, notable differences in cluster position between the two waveforms used were observed, particularly evident in **Figure 3.7c-d**. The placement of the cluster closest to the construct center for both waveforms was similar, while the locations of the remaining clusters varied significantly. Specifically, for the 0.5s dwell trapezoid waveform, nodes at the construct's corners (radial periphery and axial surfaces) formed a smaller cluster. Conversely, with the sinusoidal waveform, these clusters expanded towards the construct's center. This expansion can be attributed to the sinusoidal waveform's gradual deceleration, resulting in a decrease in fluid flux; therefor, the cluster's overall response became more aligned with the rest of the construct's response, as supported by the lower fluid flux magnitude observed in the sinusoid waveform (**Figure 3.6c-d**).

Figure 3.8 displays the average response of nodes in a cluster with absolute values for each parameter. Cluster 1, cluster 2, and cluster 3 belong to the gray, white and black cluster in **Figure 3.7**, respectively. During the end of compression, **Figure 3.8a,c,e,g**, the strain invariants (**Figure 3.8a,c**) remain relatively similar with no significant differences for any cluster between the waveforms. Similarly, the hydrostatic pressure (**Figure 3.8g**) shows no significant difference between the waveforms. The fluid flux magnitude is the exception with statistically significant

differences between cluster 2 and cluster 3. This suggests that the trapezoidal loading, which includes more abrupt transitions induces greater fluid movement within the model. The nodes closest to the radial center (cluster 1) exhibit less strain and fluid flux but more hydrostatic pressure, indicating that the center experiences more compression. Conversely, the edge (cluster 3) displays greater strain and fluid movement, likely due to the material's tendency to displace outwardly when compressed.

At the end of relaxation, **Figure 3.8b,d,f,h**, illustrate the differences between the two waveforms that are more pronounced, with cluster 2 being significantly different for all variables explored. Moreover, there are differences observed in cluster 3 for the fluid flux magnitude (**Figure 3.8f**) and the hydrostatic pressure (**Figure 3.8h**). This suggests that the relaxation phase causes more overall variation in the model's response between waveforms. Interestingly, it would be expected that the hydrostatic pressure be very low for cluster 3 based upon the zero fluid pressure boundary condition; however, there are two factors to consider. First, the reported value in the figure is an average of multiple nodal values. While cluster 3 radial center of mass is closest to the radial edge, many of the nodes are not at the radial boundary. Secondly, hydrostatic pressure within the biphasic material framework is distinct from fluid pressure and the effective stress on the solid matrix arising from the hydrostatic stress is a significant factor for consideration.

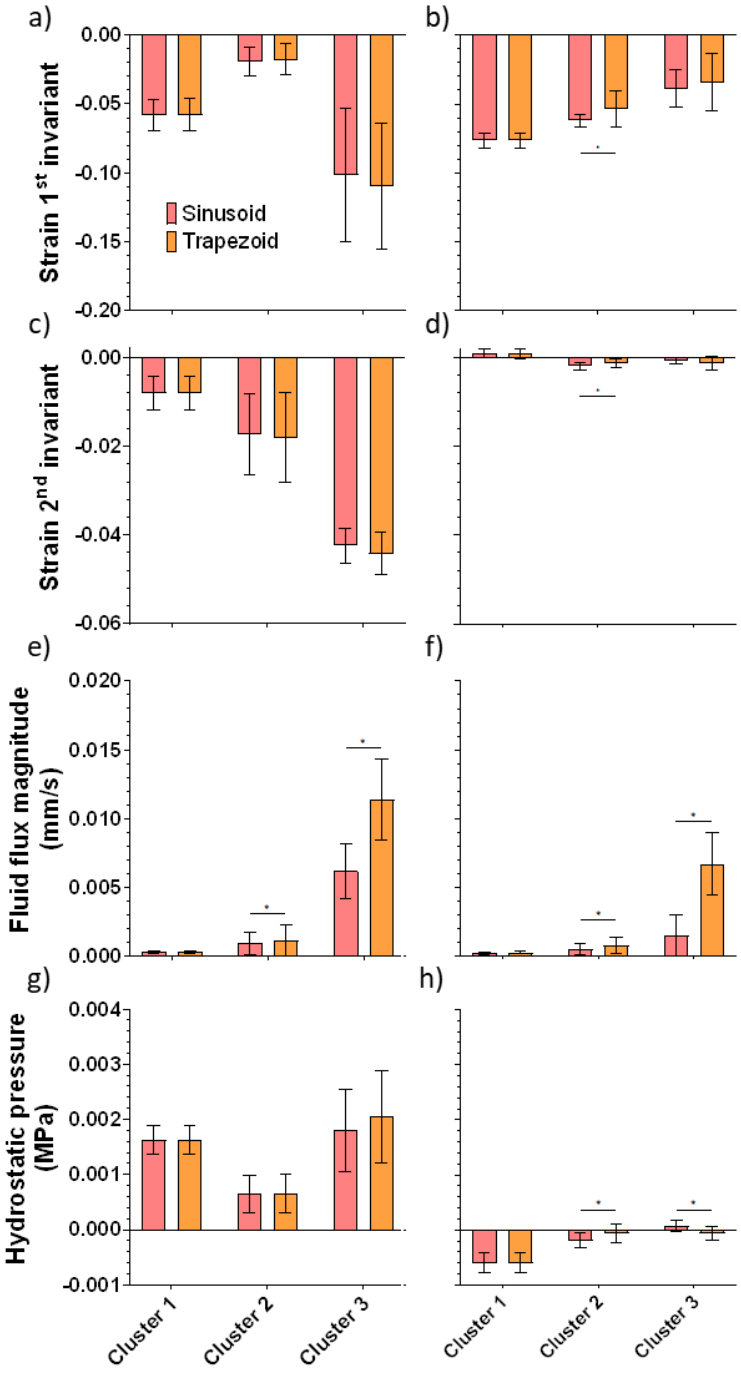

Figure 3.8: Displaying construct response by cluster for (a,b) strain 1st invariant (c,d) strain 2nd invariant (e,f) fluid flux magnitude and (g,h) hydrostatic pressure. Data is plotted at both end of compression (a,c,e,g) and end of relaxation (b,d,f,g). Errors bars are ±SD, *p<0.05 Turkey's multiple comparison test.

3.4 Conclusions

This chapter presented a method to effectively compare the spatial uniformity of cylindrical constructs cyclically loaded with different waveforms. Hydrogel constructs were modeled using FEM and analyzed by k-means clustering to reduce the dimensionality of the complex system. At the end of compression based on FEM, different waveforms had negligible effect for most of the construct expect for the magnitude of fluid flux; moreover, that single change affected a small spatial region of the construct. More differences were observed at the end of relaxation between the sinusoid waveform and the trapezoidal, but they were still heavily concentrated around the fluid flux. Constructs behaved very similarly regardless of the waveform. Additionally, that behavior could be reliably separated into three spatial domains regardless of their size. Further studies would benefit from exploring more parts of the waveform; specifically, the point of maximum velocity on a sinusoid may show little difference to the trapezoids, helping confirm the use of a trapezoid. Also, analysis of the trapezoid waveforms at the end of a dwell, instead of at the end of compression/relaxation, may produce much different responses.

Future studies could explore how different contact interfaces affect these results. The high fluid flux magnitude at the radial periphery was due to the perfectly adherent contact interface. A more challenging system with some non-zero friction would not only elicit interesting and variable responses throughout the construct but also allow the radial periphery to better relax and reduce its strain and strain rate. However, modeling such friction interfaces is not trivial. Additionally, this study did not incorporate ions into the system; osmotic pressure is an important factor in cell behavior [37]. Future model accuracy would benefit from also considering this alongside the other variables discussed. Finally, only a single waveform frequency was explored. Cells are commonly loaded with many frequencies to varied responses [29]. More investigation into how the frequency

affects construct response would be beneficial. Finally, this study explored only a cyclical compressive load. Applied loads of varied type (shear, stretch) would produce interesting results that would be appropriate in consideration to the greater goal of qualifying cellular environments when under load.

The shape and thickness of the hydrogel should also be considered. This study focused solely on a cylindrical construct, but cells have been loaded and stretched in spherical constructs [38] and in hydrogels attached to the walls of wells [39]. Such geometric differences would not only affect the overall cell environment but also the homogeneity of that response. Similar methods herein can also be applied to these varied systems. The ubiquity of FEM and ease of clustering analysis provide a framework for better evaluating what cells experience across different systems. Evaluating homogeneity was the primary focus of this study, but this approach used can be expanded to reduce the dimensions of these large spatial systems to simplify predictions.

Finally, k-means was the only algorithm used to partition the constructs into their respective clusters. Other clustering algorithms exist that may be able to provide different and more beneficial information. For example, one common algorithm similar to k-means is a self-organizing map. It has been shown that these two algorithms provide the same information [40]; however, self-organizing maps have the special ability to visualize higher-order data. While k-means clustering can map large data sets to a set of smaller discrete clusters, self-organizing maps encompass the same information while providing a lower-dimension topological map of the input. For more complicated systems, such a topological map could better elucidate the relationship between the variables that affect cell responses under loading.

Chapter 4: MSC stress response to load

4.1 Materials and Methods

A high G-block Manugel alginate (Dupont, Wilmington, DE, USA) was prepared in a 1% (w/v) solution using Dulbecco's PBS (dPBS). The solution was purified via dialysis against deionized water and sterilized by being passed through a 0.22-µm filter in sterile conditions. The resulting sterile alginate solution was then freeze-dried and stored at -80 °C for later use.

Cyclic Arg-Gly-Asp (cRGD) peptides were conjugated to the alginate via strain-promoted azide-alkyne cycloaddition (SPAAC) click chemistry as previously described [41]. Briefly, Bicyclo[6.1.0]non-4-yn-9-ylmethyloxycarbonyl]-1,8-diamino-3,6-dioxaoctane (BCN-amine; Sigma-Aldrich, St. Louis, MO, USA) was attached to the alginate as follows: First, alginate was dissolved in 0.1 M MES buffer (pH 6) and stirred for two hours before adding a mixture of EDC (Thermo Scientific) and N-hydroxysuccinimide (NHS, Fisher Scientific) followed by BCN-amine. After 24 hours of reaction at room temperature, the BCN-modified alginate was precipitated using methanol, vacuum dried, and finally re-dissolved in water and freeze-dried. The BCN-modified alginate was then prepared in dPBS, to which azide cRGD peptides were added and stirred at room temperature for 24 hours to reach a final 50µM peptide density at the end of the reaction. The solution was purified via dialysis against deionized water and sterilized by being passed through a 0.22-µm filter in sterile conditions. The resulting sterile cRGD-alginate solution was then freeze-dried and stored at -80 °C for later use.

Bone marrow-derived MSCs (RoosterBio™, Frederick, MD) were encapsulated at a concentration of 2.5×10^6/mL in 2% (wt/v) alginate or cRGD-alginate to a final cell and polymer solution at 1% (wt/v) as described previously [36]. Briefly, cell containing polymer solution was

quickly mixed with 100mM calcium sulfate and poured between two sterile glass plates with 1.5 mm spacers. The hydrogel was allowed to crosslink for one hour, and sterile 6mm diameter biopsy punch was used to form cylindrical hydrogel discs with dimension of 1.5 mm height and 6 mm diameter. The encapsulated cells were then pre-cultured in RoosterBio™ basal medium supplemented with RoosterBio™ booster for six hours. Then, hydrogel constructs were cultured in RoosterBio™ basal medium for the remainder of the study. All media were supplemented with 1% penicillin-streptomycin.

Cell-laden gels were cyclically compressed using a custom-built 24-well bioreactor as described in Chapter 2. In addition to the bioreactor shown, **Figure 4.1b**–**f** shows the individual components of a well that were used to compress a hydrogel. Constructs were compressed with a 5% strain static offset along with an 8% strain dynamic amplitude, operating at a frequency of 0.33 Hz. As discussed in Chapter 3, a trapezoidal waveform was chosen with a 0.5s dwell and 1s ramp time. After each loading cycle, platens were removed, and constructs were allowed to freely swell in the media until the next cycle began. Assay aliquots were collected from the medium after the first and third loading cycle to measure the production of nitrite products using the Griess assay (Promega, Madison, WI) according to the manufacturer's protocol. Five cRGD-alginate cell-laden gels were dissolved together, and five alginate only cell-laden gels were dissolved together to form two replicates for each condition for PCR. Each cell-laden hydrogel was considered an independent biological replicate for Griess. Nitrite concentration is presented as mean ± SD of eight or more individual gels. Comparison was made between the two timepoints – Day 0 (T1) and Day 3 (T2) for alginate and cRGD-alginate to access the effect of mechanical loading on the cells. Comparison was also made comparing cells cultured within alginate compared to those cultured within cRGD after mechanical loading to evaluate the peptide's ability to protect MSCs from mechanically induced oxidative stress.

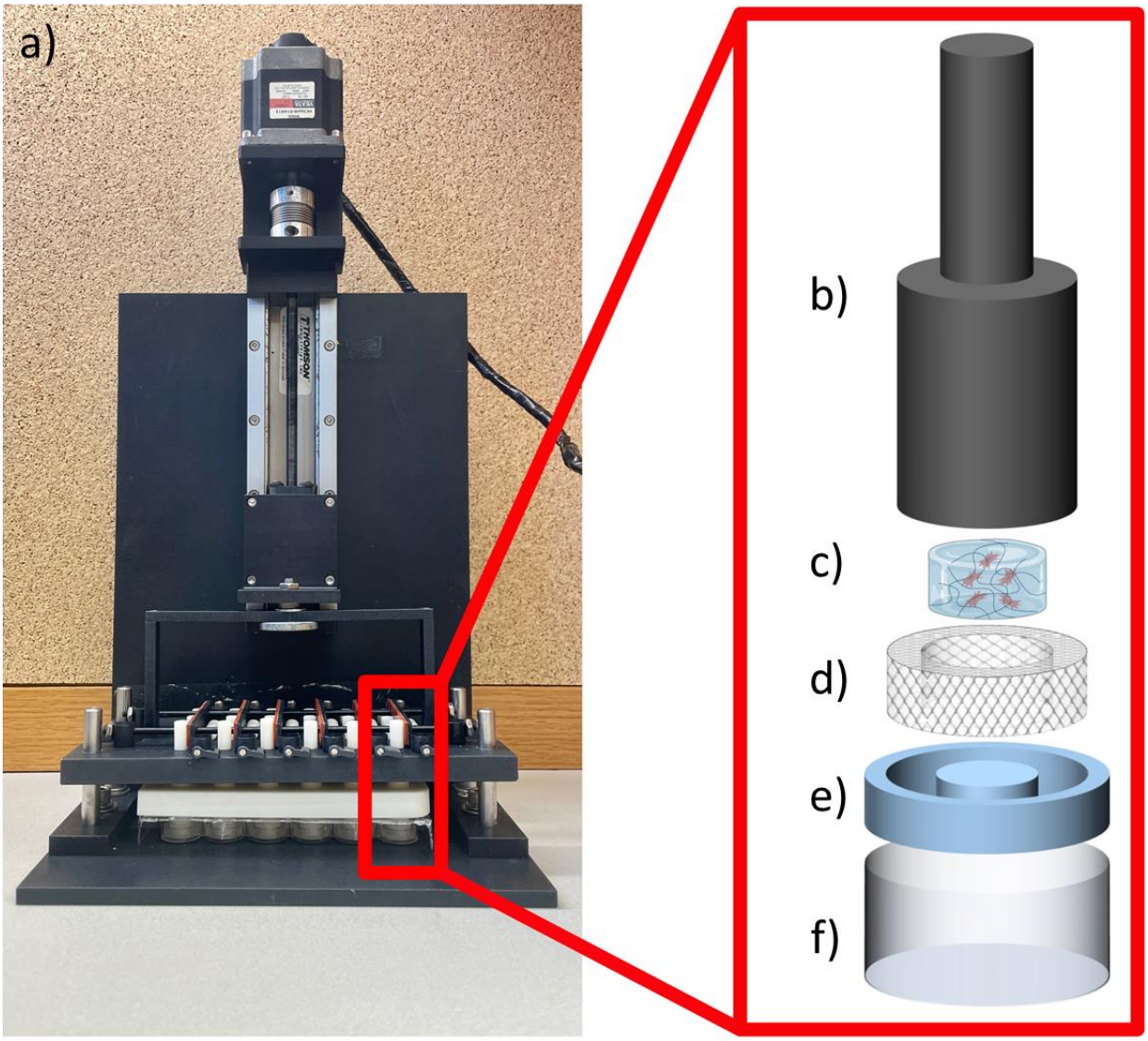

Figure 4.1: a) Mechanical loading system with individual components. b) Plastic platen. c) hydrogel. d) Porous PDMS insert for confining hydrogel and diffusing nutrients. e) Solid PDMS insert to hold porous insert and provide bottom for hydrogel. f) 24-well plate well.

4.2 Results and Discussion

Figure 4.2 shows that the medium nitrite concentration was not significantly different between cRGD-alginate and alginate with no conjugation at either timepoint; however, there is an

observable increase in medium nitrite concentration by the second timepoint. This would suggest that loading may increase the oxidative stress of the MSCs. To further investigate, PCR was performed on four targets: interleukin-6 (IL-6), a pro-inflammatory cytokine [42]; prostaglandin E_2 (PGE_2), a principal prostaglandin in inflammation [43]; cyclooxygenase (COX) 1 and COX-2, both involved in prostaglandin formation [44]. These targets all correspond to the general inflammatory and stress response of the cell.

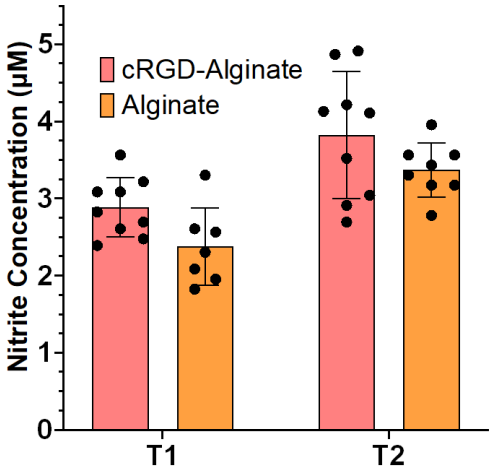

Figure 4.2: Nitrite concentration in medium at T1 and T2 for alginate with and without cRGD conjugation.

Looking at transcriptomes related to some oxidative stress genes, a trend with increase gene expression was observed for cells loaded at the second timepoint in both hydrogels for all targets except for COX1. The greatest increase was seen in the IL-6 gene, showing a four-fold increase. Except for COX-2, all targets seen to be attenuated in cRGD-alginate compared to alginate at both timepoints. Such reduction in counts for cRGD-alginate gives preliminary evidence that cRGD conjugation may be able to attenuate the stress response of MSCs when under

load; however, it is a significant limitation to have only two technical replicates for PCR. Future studies would benefit from pooling more gels. More cells would allow more definitive statements to be made.

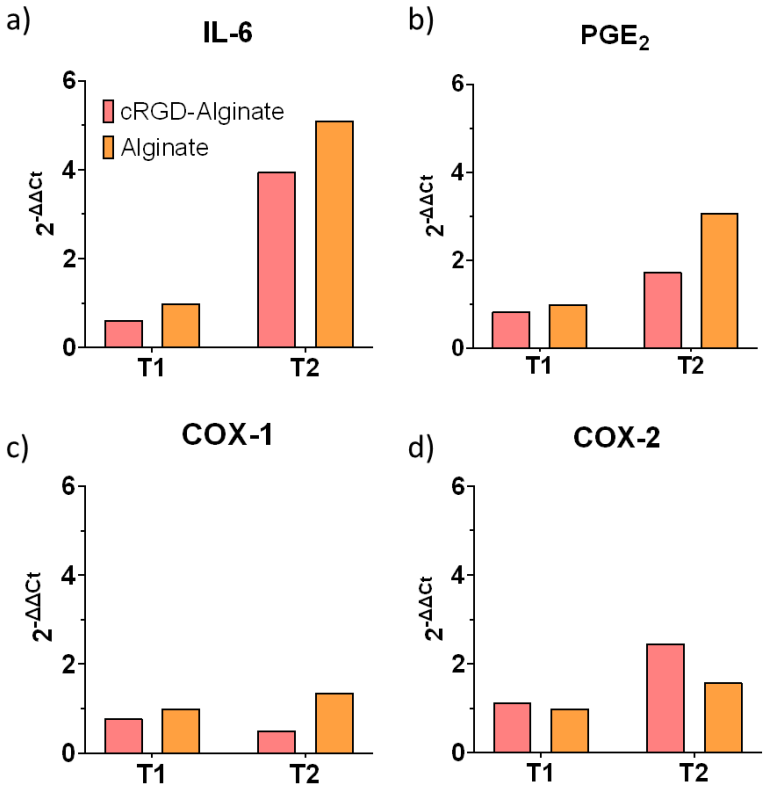

Figure 4.3: PCR for selected targets a) IL-6 b) PGE_2 c) COX-1 d) COX-2. Data is calculated from the average of ΔΔCt (n=2).

4.3 Conclusion

This study explored the mechanical stress on MSCs encapsulated in alginate hydrogels, with and without cRGD conjugation. There was increased nitrite concentrations when cells encapsulated in hydrogels were subjected to loading, as observed in previous work [45], suggesting a potential elevation in oxidative stress among MSCs. Such increases may influence the immunomodulatory

effects of MCSs [46]. To better understand the stress response of MSCs under loading, key oxidative phosphorylation markers were examined via PCR, revealing a general upsurge in oxidative stress and inflammation over time, most notably marked by an increase in IL-6 expression.

Comparison between cRGD-alginate and unmodified alginate reveals that, while nitric oxide production may not be affected, the incorporation of cRGD tends to mitigate the expression of inflammatory markers under mechanical load; however, this was not observed in COX-2. The attenuation in the cRGD-alginate group suggests a dampened cellular stress response due to the bioactive conjugation.

These findings collectively suggest that mechanical loading does indeed elevate the stress response in MSCs, as evidenced by increased nitrite and inflammatory marker expressions. However, the conjugation of cRGD to alginate hydrogels appears to offer a protective effect, attenuating the stress response and potentially enhancing the viability and functionality of MSCs within engineered constructs. These findings warranting further investigation into their mechanobiological interactions and optimization for clinical use.

References

[1] L. B. Murphy, M. G. Cisternas, D. J. Pasta, C. G. Helmick, and E. H. Yelin, "Medical Expenditures and Earnings Losses Among US Adults With Arthritis in 2013," *Arthritis Care Res (Hoboken)*, vol. 70, no. 6, pp. 869–876, Jun. 2018, doi: 10.1002/acr.23425.

[2] L. Wachsmuth and S. Söder, "Immunolocalization of matrix proteins in different human cartilage subtypes," *Histology and Histopathology*, no. 21, pp. 477–485, Feb. 2006, doi: 10.14670/HH-21.477.

[3] Y. Krishnan and A. J. Grodzinsky, "Cartilage diseases," *Matrix Biology*, vol. 71–72, pp. 51–69, Oct. 2018, doi: 10.1016/j.matbio.2018.05.005.

[4] L. J. Sandell and T. Aigner, "Articular cartilage and changes in Arthritis: Cell biology of osteoarthritis," *Arthritis Res*, vol. 3, no. 2, pp. 107–113, 2001, doi: 10.1186/ar148.

[5] D. L. Bader, D. M. Salter, and T. T. Chowdhury, "Biomechanical Influence of Cartilage Homeostasis in Health and Disease," *Arthritis*, vol. 2011, p. 979032, 2011, doi: 10.1155/2011/979032.

[6] M. B. Goldring *et al.*, "ROLES OF INFLAMMATORY AND ANABOLIC CYTOKINES IN CARTILAGE METABOLISM: SIGNALS AND MULTIPLE EFFECTORS CONVERGE UPON MMP-13 REGULATION IN OSTEOARTHRITIS," *Eur Cell Mater*, vol. 21, pp. 202–220, Feb. 2011.

[7] O.-M. Zahan, O. Serban, C. Gherman, and D. Fodor, "The evaluation of oxidative stress in osteoarthritis," *Med Pharm Rep*, vol. 93, no. 1, pp. 12–22, Jan. 2020, doi: 10.15386/mpr-1422.

[8] T. S. Ramasamy, Y. M. Yee, and I. M. Khan, "Chondrocyte Aging: The Molecular Determinants and Therapeutic Opportunities," *Front Cell Dev Biol*, vol. 9, p. 625497, Jul. 2021, doi: 10.3389/fcell.2021.625497.

[9] G. Vadalà, G. Sowa, M. Hubert, L. G. Gilbertson, V. Denaro, and J. D. Kang, "Mesenchymal stem cells injection in degenerated intervertebral disc: cell leakage may induce osteophyte formation," *J Tissue Eng Regen Med*, vol. 6, no. 5, pp. 348–355, May 2012, doi: 10.1002/term.433.

[10] F. Han *et al.*, "Tissue Engineering and Regenerative Medicine: Achievements, Future, and Sustainability in Asia," *Front Bioeng Biotechnol*, vol. 8, p. 83, Mar. 2020, doi: 10.3389/fbioe.2020.00083.

[11] S. M. Richardson *et al.*, "Mesenchymal stem cells in regenerative medicine: Focus on articular cartilage and intervertebral disc regeneration," *Methods*, vol. 99, pp. 69–80, Apr. 2016, doi: 10.1016/j.ymeth.2015.09.015.

[12] Y. Han, X. Li, Y. Zhang, Y. Han, F. Chang, and J. Ding, "Mesenchymal Stem Cells for Regenerative Medicine," *Cells*, vol. 8, no. 8, Art. no. 8, Aug. 2019, doi: 10.3390/cells8080886.

[13] N. Song, M. Scholtemeijer, and K. Shah, "Mesenchymal Stem Cell Immunomodulation: Mechanisms and Therapeutic potential," *Trends Pharmacol Sci*, vol. 41, no. 9, pp. 653–664, Sep. 2020, doi: 10.1016/j.tips.2020.06.009.

[14] Z. Lv *et al.*, "Advances in Mesenchymal Stem Cell Therapy for Osteoarthritis: From Preclinical and Clinical Perspectives," *Bioengineering (Basel)*, vol. 10, no. 2, p. 195, Feb. 2023, doi: 10.3390/bioengineering10020195.

[15] R. K. Shandil, S. Dhup, and S. Narayanan, "Evaluation of the Therapeutic Potential of Mesenchymal Stem Cells (MSCs) in Preclinical Models of Autoimmune Diseases," *Stem Cells Int*, vol. 2022, p. 6379161, Jul. 2022, doi: 10.1155/2022/6379161.

[16] J. M. Lamo-Espinosa *et al.*, "Intra-articular injection of two different doses of autologous bone marrow mesenchymal stem cells versus hyaluronic acid in the treatment of knee osteoarthritis: multicenter randomized controlled clinical trial (phase I/II)," *J Transl Med*, vol. 14, no. 1, p. 246, Aug. 2016, doi: 10.1186/s12967-016-0998-2.

[17] V. Alonso-Goulart *et al.*, "Biomaterials and Adipose-Derived Mesenchymal Stem Cells for Regenerative Medicine: A Systematic Review," *Materials (Basel)*, vol. 14, no. 16, p. 4641, Aug. 2021, doi: 10.3390/ma14164641.

[18] X. Zhao, Q. Li, Z. Guo, and Z. Li, "Constructing a cell microenvironment with biomaterial scaffolds for stem cell therapy," *Stem Cell Res Ther*, vol. 12, p. 583, Nov. 2021, doi: 10.1186/s13287-021-02650-w.

[19] A. A. El-Rashidy *et al.*, "Effect of Polymeric Matrix Stiffness on Osteogenic Differentiation of Mesenchymal Stem/Progenitor Cells: Concise Review," *Polymers (Basel)*, vol. 13, no. 17, p. 2950, Aug. 2021, doi: 10.3390/polym13172950.

[20] A. Revete *et al.*, "Advancements in the Use of Hydrogels for Regenerative Medicine: Properties and Biomedical Applications," *Int J Biomater*, vol. 2022, p. 3606765, Nov. 2022, doi: 10.1155/2022/3606765.

[21] X. Di *et al.*, "Cellular mechanotransduction in health and diseases: from molecular mechanism to therapeutic targets," *Sig Transduct Target Ther*, vol. 8, no. 1, pp. 1–32, Jul. 2023, doi: 10.1038/s41392-023-01501-9.

[22] T. Panciera, L. Azzolin, M. Cordenonsi, and S. Piccolo, "Mechanobiology of YAP and TAZ in physiology and disease," *Nat Rev Mol Cell Biol*, vol. 18, no. 12, pp. 758–770, Dec. 2017, doi: 10.1038/nrm.2017.87.

[23] R. J. Nims *et al.*, "A synthetic mechanogenetic gene circuit for autonomous drug delivery in engineered tissues," *Science Advances*, vol. 7, no. 5, p. eabd9858, Jan. 2021, doi: 10.1126/sciadv.abd9858.

[24] A. Greenwood, “mechanical_loader.” Mar. 03, 2024. Accessed: Mar. 29, 2024. [Online]. Available: https://github.com/AugustusGreenwood/mechanical_loader

[25] A. Greenwood, “stage_movement_image_analysis.” Mar. 03, 2024. Accessed: Mar. 29, 2024. [Online]. Available: https://github.com/AugustusGreenwood/stage_movement_image_analysis

[26] “Duration in time - Rust.” Accessed: Apr. 05, 2024. [Online]. Available: https://docs.rs/time/latest/time/struct.Duration.html

[27] S. K. Parashar and J. K. Sharma, “A review on application of finite element modelling in bone biomechanics,” *Perspectives in Science*, vol. 8, pp. 696–698, Sep. 2016, doi: 10.1016/j.pisc.2016.06.062.

[28] S. M. Naqvi and L. M. McNamara, “Stem Cell Mechanobiology and the Role of Biomaterials in Governing Mechanotransduction and Matrix Production for Tissue Regeneration,” *Front Bioeng Biotechnol*, vol. 8, p. 597661, Dec. 2020, doi: 10.3389/fbioe.2020.597661.

[29] C. J. O’Conor, N. Case, and F. Guilak, “Mechanical regulation of chondrogenesis,” *Stem Cell Res Ther*, vol. 4, no. 4, p. 61, Jul. 2013, doi: 10.1186/scrt211.

[30] T. Toyoda, B. B. Seedhom, J. Kirkham, and W. A. Bonass, “Upregulation of aggrecan and type II collagen mRNA expression in bovine chondrocytes by the application of hydrostatic pressure,” *Biorheology*, vol. 40, no. 1–3, pp. 79–85, 2003.

[31] P. Angele *et al.*, “Cyclic hydrostatic pressure enhances the chondrogenic phenotype of human mesenchymal progenitor cells differentiated in vitro,” *Journal of Orthopaedic Research*, vol. 21, no. 3, pp. 451–457, 2003, doi: 10.1016/S0736-0266(02)00230-9.

[32] J. Lee *et al.*, “Mechanobiological Conditioning Enhances Mesenchymal Stem Cell-Induced Vascular Regeneration,” *Nat Biomed Eng*, vol. 5, no. 1, pp. 89–102, Jan. 2021, doi: 10.1038/s41551-020-00674-w.

[33] S. C. Hicks, R. Liu, Y. Ni, E. Purdom, and D. Risso, “mbkmeans: Fast clustering for single cell data using mini-batch k-means,” *PLOS Computational Biology*, vol. 17, no. 1, p. e1008625, Jan. 2021, doi: 10.1371/journal.pcbi.1008625.

[34] S. A. Maas, B. J. Ellis, G. A. Ateshian, and J. A. Weiss, “FEBio: Finite Elements for Biomechanics,” *Journal of Biomechanical Engineering*, vol. 134, no. 011005, Feb. 2012, doi: 10.1115/1.4005694.

[35] “Osmotic Loading of Spherical Gels: A Biomimetic Study of Hindered Transport in the Cell Protoplasm - PMC.” Accessed: Apr. 04, 2024. [Online]. Available: https://www.ncbi.nlm.nih.gov/pmc/articles/PMC2828939/

[36] X. Tan *et al.*, “Integrin and syndecan binding peptide-conjugated alginate hydrogel for modulation of nucleus pulposus cell phenotype,” *Biomaterials*, vol. 277, p. 121113, Oct. 2021, doi: 10.1016/j.biomaterials.2021.121113.

[37] J. D. Finan and F. Guilak, “The effects of osmotic stress on the structure and function of the cell nucleus,” *J Cell Biochem*, vol. 109, no. 3, pp. 460–467, Feb. 2010, doi: 10.1002/jcb.22437.

[38] V. L. Thai, S. Mierswa, K. H. Griffin, J. D. Boerckel, and J. K. Leach, “Mechanoregulation of MSC spheroid immunomodulation,” *APL Bioengineering*, vol. 8, no. 1, p. 016116, Mar. 2024, doi: 10.1063/5.0184431.

[39] B. J. Stottlemire, A. R. Chakravarti, J. W. Whitlow, C. J. Berkland, and M. He, “Remote-Controlled 3D Porous Magnetic Interface toward High-Throughput Dynamic 3D Cell Culture,” *ACS Biomater. Sci. Eng.*, vol. 7, no. 9, pp. 4535–4544, Sep. 2021, doi: 10.1021/acsbiomaterials.1c00459.

[40] F. Bação, V. Lobo, and M. Painho, “Self-organizing Maps as Substitutes for K-Means Clustering,” in *Computational Science – ICCS 2005*, V. S. Sunderam, G. D. van Albada, P. M. A. Sloot, and J. Dongarra, Eds., Berlin, Heidelberg: Springer, 2005, pp. 476–483. doi: 10.1007/11428862_65.

[41] E. Jain, S. Neal, H. Graf, X. Tan, R. Balasubramaniam, and N. Huebsch, “Copper-Free Azide-Alkyne Cycloaddition for Peptide Modification of Alginate Hydrogels,” *ACS Appl Bio Mater*, vol. 4, no. 2, pp. 1229–1237, Feb. 2021, doi: 10.1021/acsabm.0c00976.

[42] G. A. Nasir *et al.*, “Mesenchymal stem cells and Interleukin-6 attenuate liver fibrosis in mice,” *Journal of Translational Medicine*, vol. 11, no. 1, p. 78, Mar. 2013, doi: 10.1186/1479-5876-11-78.

[43] J. Y. Park, M. H. Pillinger, and S. B. Abramson, “Prostaglandin E2 synthesis and secretion: The role of PGE2 synthases,” *Clinical Immunology*, vol. 119, no. 3, pp. 229–240, Jun. 2006, doi: 10.1016/j.clim.2006.01.016.

[44] F. A. Fitzpatrick, “Cyclooxygenase enzymes: regulation and function,” *Curr Pharm Des*, vol. 10, no. 6, pp. 577–588, 2004, doi: 10.2174/1381612043453144.

[45] O. F. Gardner, N. Fahy, M. Alini, and M. J. Stoddart, “Differences in human mesenchymal stem cell secretomes during chondrogenic induction,” *Eur Cell Mater*, vol. 31, pp. 221–235, Apr. 2016, doi: 10.22203/ecm.v031a15.

[46] G. Ren *et al.*, “Mesenchymal Stem Cell-Mediated Immunosuppression Occurs via Concerted Action of Chemokines and Nitric Oxide,” *Cell Stem Cell*, vol. 2, no. 2, pp. 141–150, Feb. 2008, doi: 10.1016/j.stem.2007.11.014.